

A Water-Processable and Bioactive Multivalent Graphene Nanoink for Highly Flexible Bioelectronic Films and Nanofibers

Chong Cheng,* Jianguang Zhang, Shuang Li, Yi Xia, Chuanxiong Nie, Zhenqiang Shi, Jose Luis Cuellar-Camacho, Nan Ma, and Rainer Haag*

The capabilities of conductive nanomaterials to be produced in liquid form with well-defined chemical, physical, and biological properties are highly important for the construction of next-generation flexible bioelectronic devices. Although functional graphene nanomaterials can serve as attractive liquid nanoink platforms for the fabrication of bioelectronics, scalable synthesis of graphene nanoink with an integration of high colloidal stability, water processability, electrochemical activity, and especially bioactivity remains a major challenge. Here, a facile and scalable synthesis of supramolecular-functionalized multivalent graphene nanoink (mGN-ink) via [2+1] nitrene cycloaddition is reported. The mGN-ink unambiguously displays a well-defined and flat 2D morphology and shows good water processability and bioactivity. The uniquely chemical, physical, and biological properties of mGN-ink endow the constructed bioelectronic films and nanofibers with high flexibility and durability, suitable conductivity and electrochemical activity, and most importantly, good cellular compatibility and a highly efficient control of stem-cell spreading and orientation. Overall, for the first time, a water-processable and bioactive mGN-ink is developed for the design of flexible and electrochemically active bioelectronic composites and devices, which not only presents manifold possibilities for electronic-cellular applications but also establishes a new pathway for adapting macroscopic usages of graphene nanomaterials in bionic, biomedical, electronic, and even energy fields.

The development of conductive nanomaterials for lightweight, portable, flexible, and printable electrodes, sensors, and electronic devices has attracted tremendous attention in the

electronics and energy conversion industries.^[1–4] Beyond the optoelectronics and energy devices, there is a growing interest to use these nanomaterial-based, flexible bioelectronics in various bionic and biomedical applications such as blood glucose sensors, tissue monitors, neuron-to-machine interfaces, implantable stimulators or batteries, and artificial electronic muscles and skins.^[5–11] In general, these flexible bioelectronics can be made from patterned conductive nanostructures on flexible/elastic substrates, and their functions highly rely on their intrinsic properties, such as flexibility, bendability, electric conductivity, electrochemical sensitivity, and bioactivity.^[7,12,13] Although some progress has been made, further simplification of the fabrication process and extension of their biological functionalities are urgently needed.^[7,8,14] Due to their inexpensive synthesis and wide adaptability to current manufacturing processes, liquid conductive nanoinks have become promising candidates for designing flexible bioelectronics.^[11,15,16]

Over the last decade, significant research efforts have been devoted to synthesize conductive crystals or nanomaterials in liquid phase in order to design flexible and printable electronics,^[1,5,15,17,18] including inorganic nanoparticles,^[9,19] metal nanowires,^[20]

Dr. C. Cheng, J. G. Zhang, Y. Xia, Dr. J. L. Cuellar-Camacho,
Prof. N. Ma, Prof. R. Haag
Department of Chemistry and Biochemistry
Freie Universität Berlin
Takustrasse 3, 14195 Berlin, Germany
E-mail: chong.cheng@fu-berlin.de; haag@chemie.fu-berlin.de

 The ORCID identification number(s) for the author(s) of this article can be found under <https://doi.org/10.1002/adma.201705452>.

© 2017 The Authors. Published by WILEY-VCH Verlag GmbH & Co. KGaA, Weinheim. This is an open access article under the terms of the Creative Commons Attribution-NonCommercial License, which permits use, distribution and reproduction in any medium, provided the original work is properly cited and is not used for commercial purposes.

DOI: 10.1002/adma.201705452

S. Li
Department of Chemistry
Functional Materials
Technische Universität Berlin
Hardenbergstraße 40, 10623 Berlin, Germany
C. X. Nie, Z. Q. Shi
College of Polymer Science and Engineering
State Key Laboratory of Polymer Materials Engineering
Sichuan University
610065 Chengdu, P. R. China
Prof. N. Ma
Institute of Biomaterial Science and Berlin-Brandenburg Center for
Regenerative Therapies
Helmholtz-Zentrum Geesthacht
14513 Teltow, Germany

conducting polymers,^[10] carbon nanotubes,^[18,21] and exfoliated 2D-layered nanocrystals (graphene, metal dichalcogenides, and black phosphorus).^[1,22–25] However, the development of liquid conductive nanoinks for diverse, flexible and printable electronics is still in its early stage. There are many challenges that need to be overcome before nanoinks can finally become industrial products, especially in designing electronics for bionic and biomedical fields. For instance, we need to achieve precise particle size, high colloidal stability, tailored viscosities, and non-toxic solvents in the emerging shear exfoliation or ball milling technologies.^[1]

Among the diverse conductive nanoinks that are currently being developed, low-dimensional graphene nanomaterials have been intensively explored.^[8,23,26–28] They can be easily manipulated to produce 2D conductive nanoinks in liquid phase. Meanwhile, graphene-based nanoinks (GN-inks) can be readily fabricated into different 2D and 3D composites and electronics such as electrically conductive free-standing films, patterned electronics, textiles, yarns, fabrics, elastomers, and hydrogels.^[6,28–32] Furthermore, GN-inks can be adapted to an on-demand tuning of chemical, rheological, electrical, electrochemical, and biological properties, thus making them an ever-growing class of carbon nanomaterials in designing advanced electronics.^[12,33–39] Although liquid graphene nanoinks have been successfully developed for the fabrication of bioelectronics in recent years,^[12,30,33,35,38,40] there are still many unsolved challenges in using these nanoinks in designing bioelectronics. For instance, (I) toxic and volatile organic solvents are often used; (II) they always show poor aqueous colloidal stability, thus limiting their processing on nonsolvent-resistant substrates; (III) most of currently designed GN-inks-printed devices only show high electrical conductivity; however, high electrochemical activity and sensitivity are rarely achieved and reported, especially in neutral physiological media; and (IV) there is a lack of biological cues for currently developed GN-inks to induce suitable electronic-cellular bioactivity.^[37,38,41]

Though the toxic and volatile organic solvent based GN-inks have been well established, facile and scalable synthesis of GN-inks with integrated properties of high aqueous colloidal stability, water-processability, conductivity, electrochemical-activity, and especially bioactivity have not been achieved. This even holds for more than 10 years after the discovery of graphene, which is likely due to a lack of suitable and easily scalable agents to disperse and decorate the bioinert graphene surface. In this study, we have developed a supramolecular-functionalized multivalent graphene nanoink (mGN-ink) as a novel, water-processable, and bioactive nanoink for the fabrication of flexible bioelectronics. The synthesized mGN-ink unambiguously displays a well-defined and flat 2D morphology and shows good water processability and bioactivity. The uniquely chemical, physical, and biological properties of mGN-ink endow the constructed bioelectronic films and nanofibers with high flexibility and durability, suitable conductivity and electrochemical activity, and most importantly, good cellular compatibility and a highly efficient control of stem-cell spreading and orientation.

In order to address the poor aqueous colloidal stability and lack of bioactivity of the graphene nanoink, inspired from the extracellular-matrix/heparin-mimetic structure reported in our earlier studies,^[42,43] we utilized hyperbranched polyglycerol

sulfates (HPGS) as biocompatible and multivalent electrolytes to enhance the aqueous stability of graphene nanoink by repelling $\pi-\pi$ stacking interactions and avoiding formation of graphene aggregates during chemical reduction. Meanwhile, the anchored HPGS on graphene can be used as binder to enhance carbon-to-carbon and carbon-to-substrate interactions. Furthermore, it has been reported that the strong multivalent interactions of HPGS play a key role in recognition, adhesion, and signaling processes between proteins, membranes, and cells.^[43–46] Therefore, we believed that the HPGS-functionalized graphene could be utilized as a biocompatible and bioactive nanoink for constructing bioelectronics with strong multivalent interactions and good electronic-cellular activity.

To anchor HPGS on graphene, the azide group-functionalized hyperbranched polyglycerol (HPG-N₃, ≈11% N₃ substitution ratio to OH groups, Figures S4 and S6, Supporting Information) was first anchored onto graphene oxide (GO) surface via a covalent conjugation between the azide group on HPG-N₃ and sp² carbon bonds on GO through [2+1] nitrene cycloaddition reaction at 120 °C as shown in Figure 1a and Figure S10 in the Supporting Information.^[43,47–49] It should be noted that only part of N₃ groups undergo the [2+1] cycloaddition reaction with GO. There are abundant residual N₃ groups on the graphene surface as demonstrated by IR spectrum in Figure S13 in the supporting Information. These residual N₃ groups can be further used for click conjugation with other bioactive molecules. The hydrogen bonding and hydrophobic interactions between the planar GO and HPG-N₃ are also supposed to enhance the anchoring amount of HPG on GO.^[50] It is noted that the azide-based [2+1] nitrene cycloaddition reaction provides a highly stable and fast protocol for scalable HPG functionalization and the synthesized HPG anchored graphene with low reduction degree (LRG-HPGS, LRG is the product of GO after reduction at 120 °C) can withstand long-term soaking in strong acid and basic media (Figures S13 and S14, Supporting Information).

The LRG-HPG was consecutively post-sulfated to convert bioinert HPG into biocompatible and multivalent electrolyte HPGS, namely, LRG-HPGS (Figure S15, Supporting Information). Thereafter, the LRG-HPGS was further chemically reduced by ascorbic acid (“green” reduction reagent and non-toxic) to get the highly chemically reduced mGN-inks, HRG-HPGS.^[51] To prove that our mGN-inks, HRG-HPGS, were superior to the commercially available GN-inks under aqueous conditions, we used a type of thermally reduced graphene (TRG, produced at 750 °C from GO, Figure S18, Supporting Information) as the control sample.^[52,53] Since the bare TRG was not aqueously dispersible, the TRG was accordingly functionalized with HPGS (namely, TRG-HPGS, Figure S19, Supporting Information) following similar protocol for the synthesis of HRG-HPGS.

The successful synthesis of HRG-HPGS was analyzed by the X-ray photoelectron spectroscopy (XPS, Figure 1b). The XPS spectra gave clear evidence that there were nitrogen (conjugated azide) and sulfur (sulfate groups) in the resultant 2D GN-inks, which indicated that HPG-N₃ was successfully anchored on the planar graphene. To clarify successfully chemical reduction of LRG-HPGS, the high-resolution C1s spectra for LRG-HPGS and HRG-HPGS were compared, as displayed in Figure 1c. The spectra of HRG-HPGS clearly showed that the peak intensity at

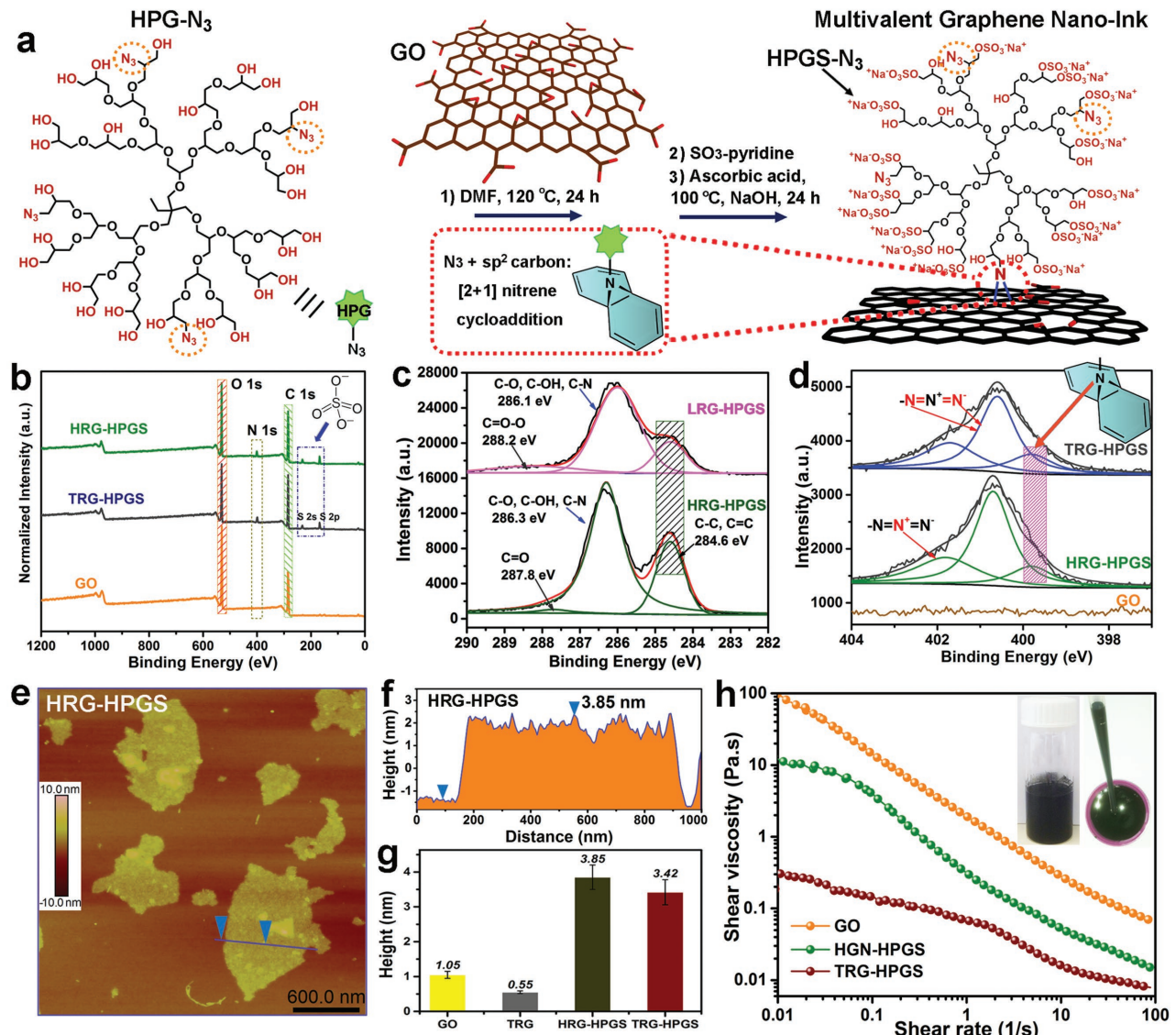


Figure 1. a) The schematic synthesis process of electrochemically active and bioactive mGN-ink, HRG-HPGS, from HPG-azide and GO via [2+1] nitrene cycloaddition reaction. b) XPS spectra for nano-inks to demonstrate the existence of nitrogen and sulfur. c) High-resolution C1s spectra for LRG-HPGS and HRG-HPGS to clarify the changes of carbon bonds after chemical reduction of LRG-HPGS. d) High-resolution N1s spectra for nanoinks to demonstrate the occurrence of [2+1] nitrene cycloaddition reaction. e, f) Representative AFM images and cross-section analyses of HRG-HPGS. g) Height profiles of GO, TRG, HRG-HPGS, and TRG-HPGS nanosheets on freshly cleaved mica, values are expressed as means \pm SD, $n = 10$. h) Viscosity dependence as a function of shear rate for graphene-based aqueous nanoinks. The inserted photograph of a glass vial was taken after standing for one month at room temperature and with a concentration of 10 mg mL^{-1} .

284.6 eV increased after chemical reduction compared to LRG-HPGS, which indicated that the graphitic network of C=C bonds was restored in HRG-HPGS.^[52] The high-resolution N1s spectra showed that the pristine GO was free of nitrogen (Figure 1d). The HPGS-N₃-conjugated graphene (HRG-HPGS and TRG-HPGS) clearly displayed nitrogen peaks, which could be deconvoluted into three peaks at 399.6–399.8 (cycloaddition-formed N-graphene conjugation), 400.7–400.9 ($=\text{N}=$ and $=\text{N}^-$ in residual N₃ groups), and 401.6–401.8 ($=\text{N}^+$ in residual N₃ groups) eV. The N1s spectra further demonstrated the high efficiency of the [2+1] nitrene cycloaddition reaction between the HPGS-N₃ and graphene nanosheets. The high chemical

reduction degree of HRG-HPGS was further clearly demonstrated by X-ray diffraction (XRD) (Figure S23, Supporting Information). The GO exhibited a characteristic peak at 11.3° . In contrast, the HRG-HPGS showed no peaks at 11.3° , which meant the oxygen groups were eliminated on GO. Meanwhile, the absence of an intensive diffraction peak at around 26° suggested that the typical π -stacking of graphene sheets had been efficiently prevented due to the decoration of HPGS. The TRG-HPGS still showed a certain degree of diffraction peak at 26° , which indicated that the nanosheets' aggregation occurred in TRG-HPGS.

The 2D morphologies of mGN-inks were characterized by atomic force microscope (AFM). As shown in Figure 1e,f,

the HRG-HPGS exhibited an extremely flat and uniform 2D morphology with an average thickness of about 3.7–3.9 nm (graphene has a AFM thickness of 0.5–0.8 nm and HPGS has an AFM thickness of 1.3–1.6 nm in dry state, Figure S9, Supporting Information), which indicated there was a uniform monolayer conjugation of HPGS on graphene nanosheets. The AFM images and height profiles of GO, TRG, and TRG-HPGS nanosheets are shown and compared in Figure 1g, which suggests that the proposed [2+1] nitrene cycloaddition reaction shows extremely good efficiency for the conjugation of multivalent supramolecular polymers on planar graphene. And it is found that there is more HPGS on HRG than TRG due to the stronger noncovalent interactions between GO and HPG (Figure S24, Supporting Information). The successful conjugation of HPGS on graphene enabled us to achieve a highly aqueous, stable mGN-ink at a high concentration up to 20 mg mL⁻¹.

The colloidal viscosity properties of GN-inks were further examined by a rheometer. The HRG-HPGS (10 mg mL⁻¹) showed a viscosity of 10–0.02 Pa s at the range of 0.01–100 s⁻¹ shear rate, which is very close to the data of the GO dispersion and much higher than the TRG-HPGS at the same concentration. Therefore, it suggests that HRG-HPGS has a similar colloidal stability as that of GO (Figure 1h). The inserted picture in Figure 1h shows a black, viscous, and stable nanoink solution of HRG-HPGS at 10 mg mL⁻¹. After standing for 1 month, there is no obvious aggregation or precipitation in the glass vial, both the size tests from dynamic light scattering and AFM analysis (Figure S26, Supporting Information) indicate that HRG-HPGS can maintain very excellent colloidal stability in long-term storage as that of pristine GO dispersion. However, the TRG-HPGS starts to aggregate after 1 d, and loses its colloidal stability and completely precipitates after 3 d of storage. The HRG-HPGS also shows much better stability in physiological media than TRG-HPGS (Figure S27, Supporting Information). These characteristics of viscosity and colloidal stability are key requirements for the ink to achieve uniform coating in different printing processes like extrusion-based printing, screen printing, and dip coating.^[54]

As shown in Figure 2a, the transmission electron microscopy (TEM) image of HRG-HPGS reveals a sheet-like and flat morphology after surface functionalization and chemical reduction, which can be compared to the exfoliated GO nanosheets (Figure S12, Supporting Information). In contrast, the TRG-HPGS exhibits a highly wrinkled and shrunken 2D morphology (Figure 2b). The higher rigidity may have been caused from the thermal reduction process of GO at 750 °C. These different nanomorphologies and rigidities may result in significantly different material properties on the macroscopic scale. To examine these different properties and performances, we utilized these mGN-inks to construct electronic films (designed as e-ink films) and ink-coated nanofibers (designed as e-ink nanofibers) as two model systems in this study. The free-standing e-ink films were made from casting mGN-inks on a Teflon dish, followed by peeling it off after drying at 45 °C. The e-ink nanofibers were made by dipcoating nanoink dispersions on O₂ plasma-treated electrospinning polycaprolactone (PCL) nanofibers.

Due to the high rigidity (\approx 1.8–2.3 GPa in stiffness, Figure S30, Supporting Information) of TRG-HPGS, the

resulting free-standing film has a rough surface (Figure S30, Supporting Information) and loose cross-sectional structure (Figure 2c). The resulting HRG-HPGS film was more soft (\approx 0.6–0.8 GPa in stiffness), flexible, and resilient against bending and rolling than the GO film (Figure 2d and Figure S28, Supporting Information). The HRG-HPGS's soft and flat 2D morphology could generate a tight “face-to-face” contact via Van der Waals interactions between the graphene sheets, which resulted in a smooth, dense, and flexible multilayer graphene film. The rigidity and flexibility not only influenced the formation of the free-standing film, it also significantly affected the structure of resulting e-ink nanofibers. From the control sample (Figure 2e), it is clearly observed that the TRG-HPGS nanoinks cannot uniformly and tightly wrap on PCL nanofibers due to their high rigidity and poor flexibility, which destroy the 3D nanofibrous morphology of substrate. For the HRG-HPGS nanoinks, as shown in Figure 2f, we demonstrate that it can be evenly coated along the PCL nanofibers with a tightly wrapped ultrathin graphene shells. Consequently, the original 3D nanofibrous morphology of PCL matrix was completely maintained. The inserted energy dispersive spectrometer (EDS) data and element mapping clearly showed the existence of abundant S from HRG-HPGS. Meanwhile the S element is also well distributed along the nanofiber, as shown in Figure 2g. The formation of a unique and fine spatial continuity of graphene shells should be attributed to the high flexibility of HRG-HPGS. The O₂ plasma treatment also helped generate abundant free radicals, which promoted the formation of a stable covalent bonding with HRG-HPGS. As shown in Figure S32 in the Supporting Information, the PCL-HRG-HPGS nanofibers showed a higher surface stiffness (Young's modulus: \approx 0.8–1.0 GPa) than pure PCL nanofibers (\approx 0.3–0.5 GPa).

Earlier reports indicated that it was possible to coat GO dispersion on textiles, yarns, and electrospinning nanofibers in order to design e-ink nanofibers.^[34,36] The Kim group proposed a way to fabricate electronic textiles by coating GO onto nylon-6, cotton, and polyester using bovine serum albumin (BSA) as an electrostatic glue.^[32] However, using BSA to facilitate the GO coating can lead to thermal instability, biodegradation, and additional pH controlling. The direct drop-casting of GO dispersion on most textiles, fabrics, and electrospinning nanofibers would result in a dense GO film and disrupted 3D morphology due to the poor compatibility between GO and polymeric substrates and strong interactions between GO nanosheets (Figure S35, Supporting Information).^[6,34] The vacuum-assisted coating process can only solve the problem for small substrates and is not adapted to large-size fabrication and thus is more costly. Most importantly, the further chemical reduction of GO is always needed in these cases, which may introduce potential contamination of toxic chemical molecules.^[6,32,34] In our protocol, no further chemical reduction is needed, and the preferable nanofibrous architecture of PCL nanofibers is completely maintained, which may be beneficial for applications where 3D geometrical morphology of substrates is highly needed. Moreover, the GN-inks-based coating protocol may also be used as a highly efficient graphene layer protection strategy to design stable Li-S and Li-ions batteries.^[55]

The flexibility and robust mechanical properties of the free-standing e-ink films were further validated by tensile

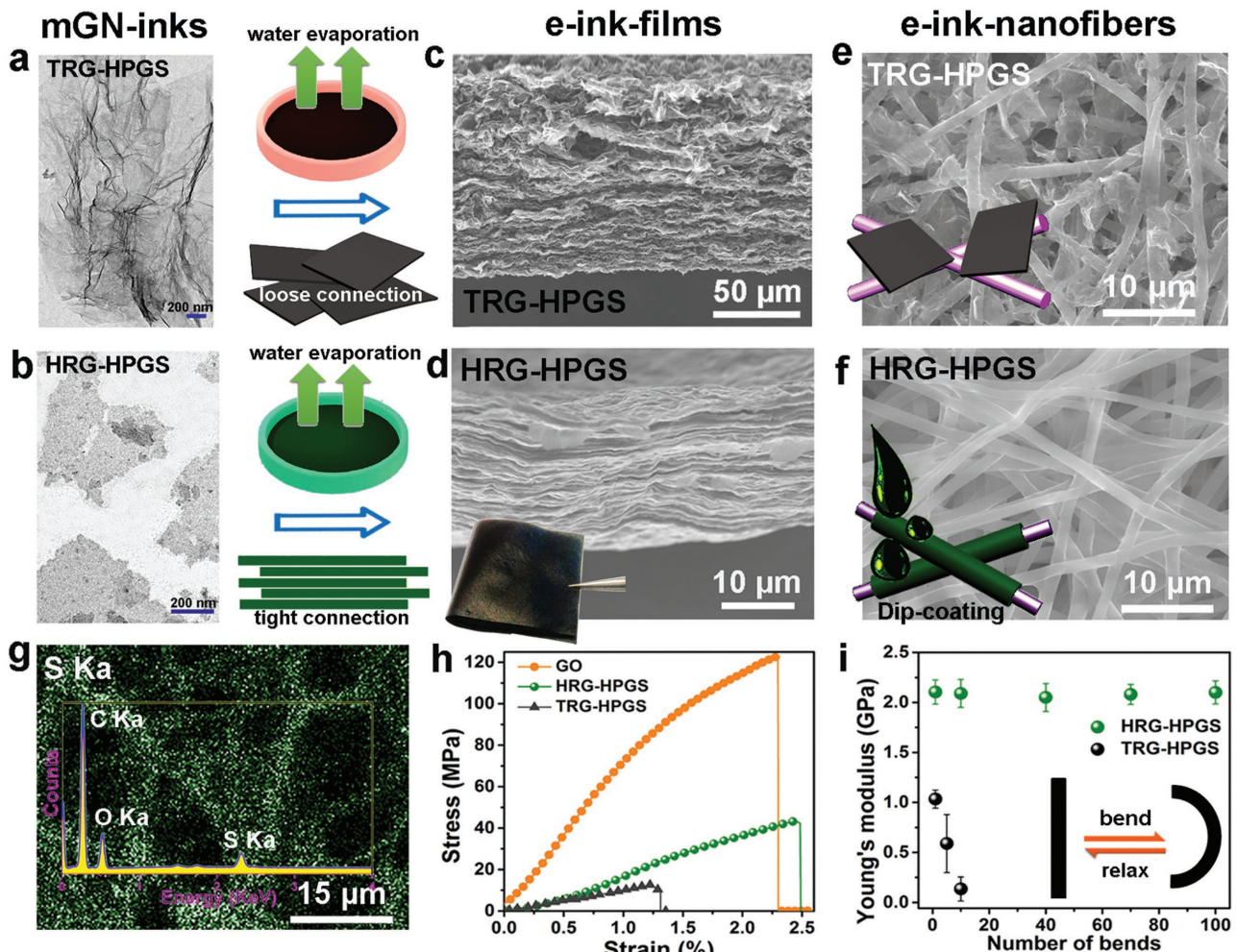


Figure 2. Typical TEM images of TRG-HPGS a) and HRG-HPGS b) nanosheets from aqueous dispersions. c) Cross-sectional SEM images of PCL-TRG-HPGS e-ink films. Note: all the PCL nanofibers were treated with O₂ plasma to generate radicals and form stable covalent bonding with mGN-inks. d) Cross-sectional SEM images of the PCL-HRG-HPGS, inserted photograph: HRG-HPGS free-standing e-ink films. The surface SEM images of the PCL-TRG-HPGS e) and PCL-HRG-HPGS free-standing e-ink nanofibers f). g) The SEM element mapping and EDS curves of the PCL-HRG-HPGS. The tensile machine-tested mechanical properties of the free-standing e-ink films from different nanoinks, h) stress-strain curves, and i) long-term mechanical stability of the film under bending, values are expressed as means \pm SD, $n = 3$.

measurement. Interestingly, GO film exhibited the highest tensile strength (120 ± 5 MPa) and ultimate elongations of 2.2%–2.3%. The HRG-HPGS film showed 3 times lower tensile strength than the GO film (40 ± 2 MPa) and ultimate elongations of 2.5–2.6%, (Figure 2h). The mechanical performance of HRG-HPGS was much better than the TRG-HPGS (10 ± 1 MPa, 1.5–1.6% elongation). The mechanical stability after cycling bends further showed that HRG-HPGS presented much better long-term durability than TRG-HPGS (Figure 2i).

The electrical conductivities of the dried free-standing e-ink films and e-ink nanofibers were then tested. The HRG-HPGS-based e-ink film had a conductivity of ~ 900.0 S cm⁻¹, which was much higher than the GO-based e-ink film (~ 0.2 S cm⁻¹), but 6 times lower than the TRG-HPGS-based e-ink film (~ 5200.0 S cm⁻¹, Figure 3a). The relative lower conductivity of HRG-HPGS should be attributed to the higher conjugation density of HPGS (Figure S24, Supporting Information), which increased the junction resistance between graphene

sheets. Meanwhile, the TRG treated at 750 °C was naturally more conductive than the ascorbic acid-reduced HRG. Besides the high conductivity, another important target for designing flexible e-ink films for practical applicability is preserving the electrical conductivity during bending and folding. As shown in Figure 3b, no conductivity loss is observed for HRG-HPGS after bending 100 times due to its flexible, dense, and tight-layer structure. However, the loose-layered structure of TRG-HPGS dramatically decreased in conductivity during bending. The TRG-HPGS film was broken after bending 10 times and completely lost the conductivity.

To test the conductivity of different e-ink nanofibers, mGN-ink-coated electronic fabric, cellulose paper, and electrospinning PCL nanofibers were fabricated with the same loading amount of nanoink. The HRG-HPGS-based e-ink nanofibers all showed higher electrical resistivity, ranging from 400 ± 50 to 700 ± 80 Ω cm, than the TRG-HPGS-based ones (Figure 3c). However, the HRG-HPGS-based e-ink nanofibers were conductive enough

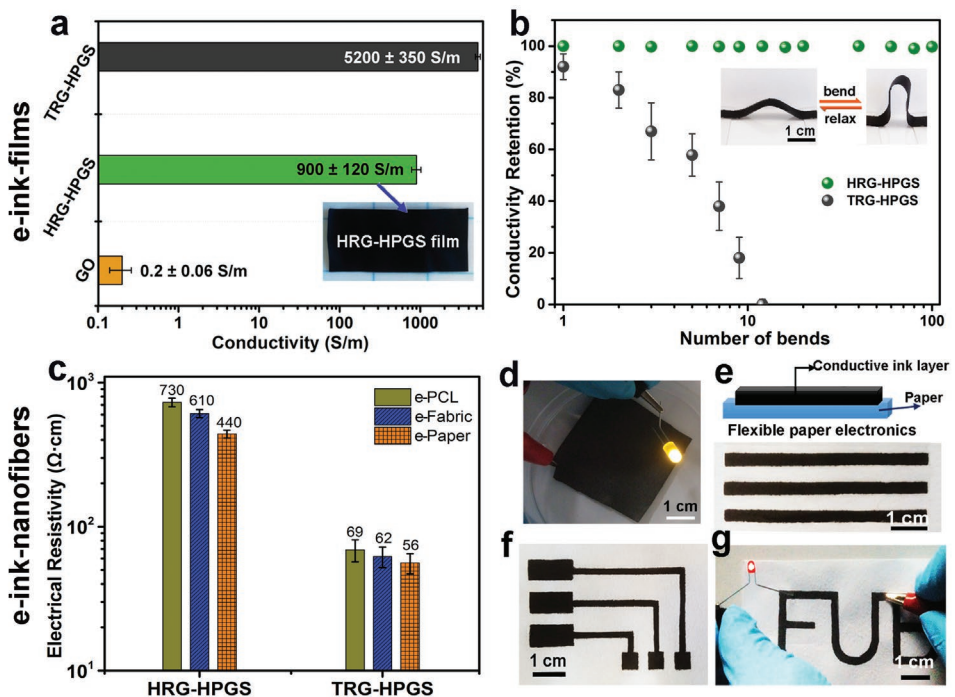


Figure 3. a) Electrical conductivity of free-standing e-ink films. b) Electrical characteristics of free-standing e-ink films during bending and relaxing deformation for 100 times. c) Electrical resistivity of 3D conductive e-ink nanofibers. d) Inserted photograph shows a lighted LED connected by HRG-HPGS coated fabric. e–g) Fabrication of HRG-HPGS nanoink-based paper electronics in different patterns by brush-printing method with a plastic mask on cellulose paper. Values are expressed as means \pm SD, $n = 4$.

to turn on a light-emitting diode (LED) by applying an extra 3.0 V potential (Figure 3d). The above result revealed that the HRG-HPGS would have satisfactory electrical conductivity and high stability during the usage. Meanwhile, considering that the proposed method is cheap and easy to handle, it is believed that the HRG-HPGS nanoinks may be further employed to make wearable electronic textiles. Furthermore, the synthesized mGN-inks are also adaptable to other current manufacturing processes, for instance, brush printing. Using the mask-based brush-printing technique, we deposited HRG-HPGS nanoinks on cellulose paper with various predefined patterns, such as aligned stripe, two-point electrode, and the FUB logo (Figure 3e–g). The HRG-HPGS nanoink showed extremely strong adhesion to the paper substrate, which would facilitate the printing process and result in robust and flexible paper electronics. Meanwhile, this conductive mGN-ink is water-processable, which will not damage the polymeric substrates compared to commercially used GN-inks dispersed by organic solvents. However, due to the good solubility of the HPGS crown polymer in diverse organic solvents, the synthesized HRG-HPGS can be easily dispersed in organic solvents to form a homogenous nanoink, such as methanol, ethanol, and dimethylformamide. Since the organic solvent dispersed graphene nanoink is compatible to inkjet printing or screen printing,^[1] it is possible to use this GN-ink for designing organic solvent-based printable and scalable bioelectronic device applications, which will be discussed in detail in a future report.

To assess the electrochemical activity of mGN-inks and their potential applications as bioelectronics, such as neural monitor, biocapacitors, and biosensors, cyclic voltammetry (CV) was

performed in neutral physiological media (phosphate-buffered saline (PBS) buffer or cell culture medium). In Figure 4a and Figure S42 in the Supporting Information, the CV curves of HRG-HPGS nanoinks on a glass carbon electrode (GCE) show good electrochemical capacitance and rate performance in PBS buffer. Compared to HRG-HPGS, the bare GCE and TRG-HPGS nanoink exhibited much smaller electrochemical capacitance, which indicated that HRG-HPGS nanoink was a better ionic conductor and accumulated much more electrical double-layer capacitance than the TRG-HPGS ink.

The electrochemical impedance performance of bioelectrodes is also a determining factor when one evaluates their electrical resistance and ionic transfer characteristics. The lower impedance (Z) values indicated that the nanoink-based electronics would have excellent application performance like in electrophysiological signal recording and bioelectrical stimulation. Figure 4b shows the impedance curves measured by a frequency response analyzer from 10 to 10^5 Hz. The HRG-HPGS has lower and more stable Z values than TRG-HPGS for the entire spectrum. Although the conductivity measurements with a standard four-point probe show that the HRG-HPGS has higher electrical resistivity than TRG-HPGS, the lower Z values of HRG-HPGS may be a result from its flexible and densely layered structures. The higher Z values of TRG-HPGS could have been caused by its more rigid and rougher structure that led to poor interfacial contact with the GCE electrode and resulted in higher Z values. For the Nyquist plots (Figure 4c), small arcs at high frequencies (process limited by electron transfer) and straight lines in the low frequency region (ion diffusion-limited electron transfer) are observed, which indicates the charge

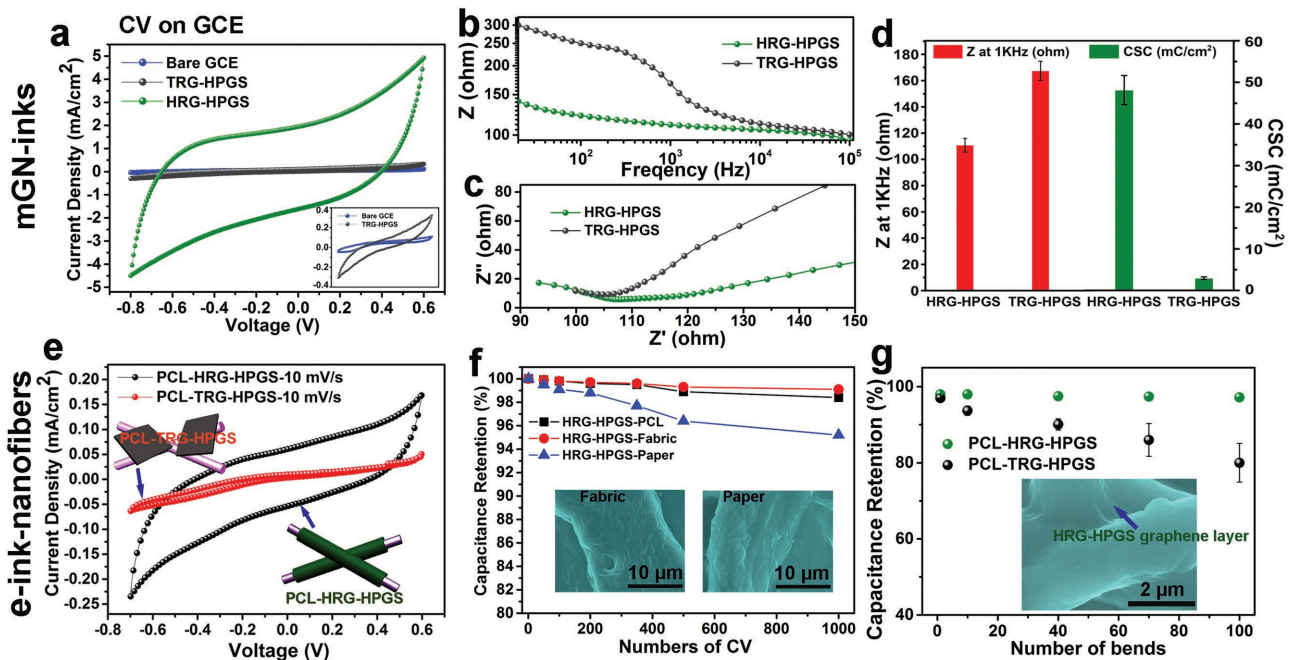


Figure 4. Electrochemical behavior of mGN-inks and resulting e-ink nanofibers in a three-electrode electrochemical setup. a) CV curves of HRG-HPGS and TRG-HPGS mGN-inks on GCE and bare GCE, 50 mV s^{-1} . b) Overall impedances of mGN-inks on GCE in PBS from 10 to 10^5 Hz , 25 mV s^{-1} . c) Nyquist plots of mGN-inks on GCE in PBS. d) Impedances of mGN-inks on GCE in 1 kHz in PBS, and the values of total CSC for each mGN-ink at 50 mV s^{-1} . e) CV curves of the e-ink-nanofibers in DMEM medium, 10 mV s^{-1} . f) Capacitance retention ratios of different HRG-HPGS ink-coated electronic nanofibers over long-term CV scanning in DMEM medium. g) The capacitance retention ratios after different bending cycles in DMEM medium. Values are expressed as means \pm SD, $n = 4$.

transfer procedure in nanoinks is controlled both by electron transfer and ion diffusion. The steeper gradient of TRG-HPGS at low frequency region depicts that it has a faster ion diffusion rate due to its loosened graphene layers. Overall, these observations demonstrate that the HRG-HPGS nanoinks has a charge-transfer resistance similar to other carbon nanomaterials and conductive polymers.^[15,56]

The impedance (Z) at 1 kHz is an important parameter that relates to the frequency of cellular recording and power consumption during electrical stimulation.^[56] In Figure 4d, the Z values at 1 kHz of HRG-HPGS outperform the TRG-HPGS ink. The total cathodic charge storage capacity (CSC) is also quite informative for evaluating the performance of bioelectronic devices. The CSC value of HRG-HPGS ink ($48.1 \pm 3.5 \text{ mC cm}^{-2}$) is almost 16 times higher than the TRG-HPGS ink ($3.0 \pm 0.3 \text{ mC cm}^{-2}$). The total CSC of the HRG-HPGS on GCE is superior to many of the earlier studies and can compete with the best reported data, for example, for the gold nanoparticles (2.5 mC cm^{-2}),^[19] carbon nanotubes ($2.2\text{--}2.5 \text{ mC cm}^{-2}$),^[21] and PEDOT-GO on gold electrodes ($10\text{--}80 \text{ mC cm}^{-2}$).^[56] But we should also note that this evaluation was not based on the same standard, including thickness, medium, and also working electrodes.

Besides the inherent electrochemical performance of the nanoinks, we further measured the electrochemical activity of mGN-ink-based paper electronic and e-ink nanofibers. In Figure S45 in the Supporting Information, the CV curves of both HRG-HPGS-patterned paper electronic and e-ink nanofibers displayed excellent rate performances and rectangular-like

shapes. As shown in Figure 4e, the e-ink nanofiber of PCL-HRG-HPGS exhibited a much higher charge capacitance than the PCL-TRG-HPGS. These data further validated that HRG-HPGS had a superior electrochemical performance with good electrical double-layer capacitance between graphene ink and electrolyte interface. The CV curves and long-term stabilities of HRG-HPGS based e-ink-nanofibers were carried out and are shown in Figure 4f. All the samples maintained 95% capacitances after 1000 times cycling CV measurements. Furthermore, the e-ink-nanofiber of PCL-HRG-HPGS also showed extremely stable capacitance over 100 times of bending and no obvious dissociation of HRG-HPGS coating layers is occurred (Figure 4g). This good capacitance resistance to shape deformation can be attributed to the strong binding and adhesion between HRG-HPGS ink and O₂ plasma-treated electrospinning nanofibers. Therefore, we believe that the good electrochemical activity of HRG-HPGS in physiological media will enable the creation of stable bioelectronics for diverse bionic and biomedical applications.

A major drawback for many commercial conductive inks is their potential cell toxicity and lack of biological cues to induce suitable electronic-cellular bioactivity. The cellular cytocompatibility and bioactivity are systematically evaluated to clarify whether the engineered conductive HRG-HPGS nanoinks can be applied as biocircuits, biosensors, or implantable electronics. In this study, we utilized the human adipose-derived mesenchymal stem cells (hADMSC) as a bifunctional model system, which could not only provide a highly vulnerable and sensitive cell line to assess the cytocompatibility, but also allow

for further bioactivity investigations of nanoink-based bioelectronics on stem cell adhesion, spreading, orientation, and even differentiation. As shown in Figure 5a and Figures S46 and S47 in the Supporting Information, the results of live-dead staining indicated that GO and TRG-HPGS nanoinks showed significantly fewer live cells compared to tissue culture polystyrene (TCPS). Meanwhile, the HRG-HPGS showed a similar live cell ratio as TCPS, which demonstrates its good cytocompatibility. For the live-dead ratios of hADMSC on e-ink films, the HRG-HPGS-based e-ink film had a 90% live cell ratio compared to TCPS, which meant there was a good cell viability that

was significantly better than all other e-ink films (Figure S48, Supporting Information). Furthermore, compared to bare PCL, PCL-GO, and PCL-TRG-HPGS, the PCL-HRG-HPGS has much higher cell compatibility (Figure 5b), and the cell adhesion and spreading on PCL-HRG-HPGS is also better than the other nanofibers as indicated by F-actin staining (Figure S51, Supporting Information). It is believed that the excellent cytocompatibility of HRG-HPGS should be benefited from its extracellular matrix-mimetic chemical structures. Besides the cytocompatibility, we also demonstrated that the residual N₃ groups on HRG-HPGS nanoinks could be further post-functionalized

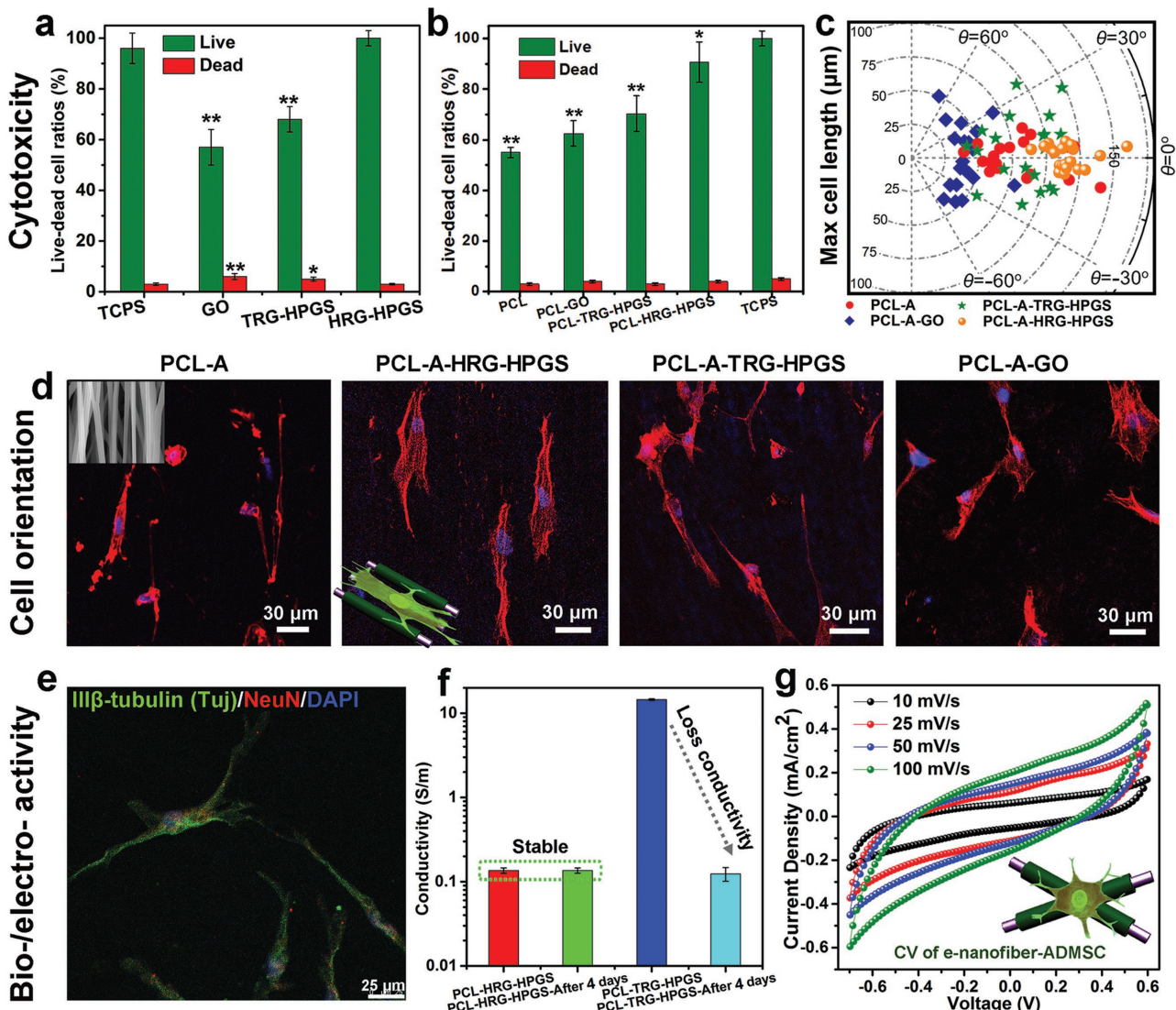


Figure 5. Cellular behaviors of the nanoinks and engineered e-ink-nanofibers. a) Live-dead cell ratios of hADMSC after being incubated with different nanoinks ($20 \mu\text{g mL}^{-1}$) for 1 d. b) Live-dead cell ratios of hADMSC after being seeded on different nanoink-coated PCL nanofibers. Values are expressed as means \pm SD, $n = 20$, $*p < 0.05$ and $**p < 0.005$ versus bare TCPS. c) The quantitative analysis of cellular orientation distribution on the engineered e-ink-nanofibers. θ ($^{\circ}$) is the angle subtended by the long axis of the cell and the radius is defined as the maximal cell length of each cells. d) Typical confocal laser scanning microscopy (CLSM) images of hADMSC on bare PCL-A nanofiber and nanoink-coated PCL-A; cells were stained with F-actin (phalloidin-647) and cell nuclei (DAPI). e) Fluorescent images of hADMSC on PCL-HRG-HPGS substrates after 4 d culture showing the loss of “stemness” and beginning of neural differentiation. (Green: the neuronal marker protein of III β -tubulin (Tuj) for microtubule element and filopodia; red: neuron-specific nuclear and cytoplasm marker protein, NeuN, for intermediate and mature neurons; blue: DAPI staining for nuclear). f) Conductivity change of engineered e-ink-nanofibers after 4 d cell culture experiments, error bars show the standard error of the mean from 3 tests. g) CV curves of the HRG-HPGS-based e-ink-nanofibers after 4 d cell culture experiments in DMEM medium.

with RGD peptide by azide-alkyne cycloaddition reaction, the RGD conjugated HRG-HPGS-based e-ink nanofiber had much higher live cell ratio than HRG-HPGS-based one (Figure S52, Supporting Information). It suggested that the mGN-inks could be further endowed with desired and functional ligands with specific bioactivity via facile click reaction.

Beyond the cytocompatibility and bioactivity achieved from the specific chemical structures of nanomaterials, in earlier reports, nanomaterials can also be utilized to control the physical cues of substrates such as nanotopographical features, substrate stiffness, and geometry for different biological applications.^[14,34,36,57] It has been reported that the precisely controlled substrate's morphologies on the sub-micrometer to micrometer scale were suitable for controlling cellular morphology, spreading, orientation, phenotype, and differentiation. Ariga et al. suggested that highly ordered fullerene crystals could be used for macroscopic controlling of myoblast orientation and enhancement of myogenic differentiation; the myoblasts on the aligned substrates grew and elongated their shape and fused to form multinuclear myotubes.^[58] The Lee group demonstrated a nanotopographical features consisting of GO and silica nanoparticle could be used for the alignment and extension of neural axons, the engineered microenvironment provided instructive physical cues for enhanced neuronal differentiation from hNSCs.^[59]

In our above studies, we have demonstrated that the HRG-HPGS nanoink was able to form a tight, uniform, and ultrathin carbon layers along the electrospinning PCL nanofiber and that the original nanofibrous geometrical features can be completely maintained (Figure 2d for random and Figure S34, Supporting Information for aligned e-ink nanofibers). Therefore, we investigated the stem-cell orientation activity of the aligned PCL nanofiber (PCL-A) and HRG-HPGS nanoink coated PCL-A, Figure 5c,d. To quantify the orientation and elongation of hADMSC on substrates, we calculated the cell variation in the angle of orientation, θ ($^{\circ}$), (Figure 5c). Both the bare PCL-A and PCL-A-HRG-HPGS nanofibers exhibit uniform cell alignment along with the fiber direction, the variation in orientation angles of hADMSC are within $\pm 16^{\circ}$ and $\pm 10^{\circ}$, respectively. Due to the poor 3D nanofibrous geometrical features after coating of GN-inks, the PCL-A-TRG-HPGS could induce certain degree cell orientation (within $\pm 35^{\circ}$), while the PCL-A-GO could not induce significant cell orientation ($\pm 65^{\circ}$) (Figure S35, Supporting Information). On the other hand, no cell alignment was observed for all the random PCL nanofibers (Figure S51, Supporting Information). For the max cell extending lengths of GN-ink-coated nanofibers, the cells on PCL-A-HRG-HPGS are much longer than the bare PCL-A, PCL-A-TRG-HPGS, and PCL-A-GO surfaces. Meanwhile, the cells on PCL-A-HRG-HPGS also have much larger cell extending length compared to the cells on random PCL-HRG-HPGS (Figure S51, Supporting Information). Therefore, we confirmed that the HRG-HPGS nanoink could serve as exclusively biocompatible and bioactive coating reagent to guide stem cell orientation and morphologies, which not only had ECM-like structures, but also showed no influence on the original geometrical and physical features of substrates.

Due to the neural differentiation potential of hADMSCs, in the study, we further examined the stem cell phenotype after

4 d culture on the substrate. It was interesting to find out that the adhered hADMSCs gradually lost their "stemness" properties and started the neural differentiation with the production of typical neural markers on PCL-HRG-HPGS nanofibers (Figure 5e and Figure S53, Supporting Information), which suggested that the e-ink nanofibers could also serve as a vital tool to control the differentiation of electrically excitable cells, especially for neural induction because of the conductive characteristics and these nanofibers' close morphological resemblance to neurites of neurons.^[34,59] In our next study, we will give a detailed report on the in vitro differentiation responses of hADMSC on PCL-HRG-HPGS nanofibers and clarify the effects of conductive microenvironment, aligned-random geometry cue, and electrical stimulation on neural differentiation of stem cells.

After sterilization and soaking in cell culture medium for 4 d, the conductivity stability of engineered e-ink nanofibers was tested again. It was found that the conductivity of PCL-HRG-HPGS was very stable, while, the PCL-TRG-HPGS had a very dramatic conductivity loss after usage due to the unstable surface coating structure and dissociation of graphene sheets (Figure 5f). The HRG-HPGS-based e-ink nanofibers also had very stable electrochemical activity after soaking in cell culture medium compared to the original one (Figure 5g and Figure S55, Supporting Information). Overall, the HRG-HPGS-based e-ink nanofibers combine with chemical bioactivity and specific nanotopographical features induced physical bioactivity, which may provide a novel and powerful tool for many future studies, such as cell morphology guidance, stem cell differentiation controlling, artificial muscle, spinal nerve repair, and electronic implants.

In conclusion, for the first time, we have successfully developed a multivalent supramolecular-functionalized, conductive, water-processable, and bioactive GN-ink by a facile and scalable strategy. This nanoink exhibits a well-defined and flat 2D morphology, extremely good stability in water and biological fluids, good adaptability to conventional coating/printing processes, and good cytocompatibility. The uniquely chemical, physical, and biological properties of mGN-ink endow the constructed bioelectronic films and nanofibers with high flexibility and durability, suitable conductivity and electrochemical activity, good cellular compatibility, and a highly efficient control of stem-cell spreading and orientation. Notably, this is the first study to report a highly facile strategy for fabricating conductive bioelectronic nanofibers with excellent flexibility, a uniform 3D morphology, and good geometrical bioactivities on the alignments and orientations of hADMSC. In our protocol, no further chemical reduction is needed, the preferable nanofibrous architecture can be completely maintained, and most importantly, the e-ink nanofibers show a very robust and durable conductivity and electrochemical activity under physiological condition. Overall, it is believed that the developed mGN-ink has great potential for designing flexible, electrochemically active and bioactive electronic devices or composites for various electronic cellular applications, i.e., in vivo tissue recording and spatiotemporal monitoring, cellular/pathogen signal detection, electrical circuit, regulation of stem-cell growth, orientation and differentiation, neural induction and stimulation. We also expect that this novel protocol of synthesis of mGN-ink will start a new pathway for

adapting the macroscopic usages of graphene nanomaterials in bionic, biomedical, electronic, and even energy fields.

Experimental Section

Experimental details including materials, characterizations, and synthesis of multivalent graphene nanoinks, preparation of bioelectronic films and nanofibers, conductivity and electrochemical activity, stem-cell culture, and bioactivity tests are listed in the Supporting Information.

Supporting Information

Supporting Information is available from the Wiley Online Library or from the author.

Acknowledgements

The authors gratefully acknowledge financial assistance from Deutsche Forschungsgemeinschaft (DFG) through grants from the Collaborative Research Center (SFB) 765 and 1112, Helmholtz Virtual Institute on "Multifunctional Biomaterials for Medicine." C.C. acknowledges the support of the DRS POINT Fellowship of Freie Universität Berlin, and an Alexander von Humboldt Fellowship. Ievgen S. Donskyi is acknowledged for discussion in nanoink's characterizations. Dr. Pamela Winchester is sincerely acknowledged for language polishing the manuscript.

Conflict of Interest

The authors declare no conflict of interest.

Keywords

cellular bioactivity, conductive nanoinks, cytocompatibility, flexible bioelectronics, supramolecular-functionalized multivalent graphene

Received: September 20, 2017

Revised: October 11, 2017

Published online: December 11, 2017

- [1] F. Bonaccorso, A. Bartolotta, J. N. Coleman, C. Backes, *Adv. Mater.* **2016**, *28*, 6136.
- [2] S. Li, C. Cheng, A. Thomas, *Adv. Mater.* **2017**, *29*, 1602547.
- [3] S. G. Hashmi, D. Martineau, M. I. Dar, T. T. T. Myllymaki, T. Sarikka, V. Ulla, S. M. Zakeeruddin, M. Gratzel, *J. Mater. Chem. A* **2017**, *5*, 12060.
- [4] J. Gong, M. Antonietti, J. Yuan, *Angew. Chem., Int. Ed.* **2017**, *56*, 7557.
- [5] J. Zhu, M. C. Hersam, *Adv. Mater.* **2017**, *29*, 1603895.
- [6] J. W. Jeon, S. Y. Cho, Y. J. Jeong, D. S. Shin, N. R. Kim, Y. S. Yun, H. T. Kim, S. B. Choi, W. G. Hong, H. J. Kim, H. J. Jin, B. H. Kim, *Adv. Mater.* **2017**, *29*, 1605479.
- [7] Y. S. Rim, S. H. Bae, H. Chen, N. De Marco, Y. Yang, *Adv. Mater.* **2016**, *28*, 4415.
- [8] C. Cheng, S. Li, A. Thomas, N. A. Kotov, R. Haag, *Chem. Rev.* **2017**, *117*, 1826.
- [9] H. Zhang, J. Shih, J. Zhu, N. A. Kotov, *Nano Lett.* **2012**, *12*, 3391.
- [10] C. Yu, C. Wang, X. Liu, X. Jia, S. Naficy, K. Shu, M. Forsyth, G. G. Wallace, *Adv. Mater.* **2016**, *28*, 9349.
- [11] J. Gong, H. Lin, J. W. C. Dunlop, J. Yuan, *Adv. Mater.* **2017**, *29*, 1605103.
- [12] H. Jang, Y. J. Park, X. Chen, T. Das, M. S. Kim, J. H. Ahn, *Adv. Mater.* **2016**, *28*, 4184.
- [13] D.-H. Kim, N. Lu, R. Ma, Y.-S. Kim, R.-H. Kim, S. Wang, J. Wu, S. M. Won, H. Tao, A. Islam, K. J. Yu, T.-i. Kim, R. Chowdhury, M. Ying, L. Xu, M. Li, H.-J. Chung, H. Keum, M. McCormick, P. Liu, Y.-W. Zhang, F. G. Omenetto, Y. Huang, T. Coleman, J. A. Rogers, *Science* **2011**, *333*, 838.
- [14] P. Wang, J. Sun, Z. Lou, F. Fan, K. Hu, Y. Sun, N. Gu, *Adv. Mater.* **2016**, *28*, 10801.
- [15] S. R. Shin, R. Farzad, A. Tamayol, V. Manoharan, P. Mostafalu, Y. S. Zhang, M. Akbari, S. M. Jung, D. Kim, M. Comotto, N. Annabi, F. E. Al-Hazmi, M. R. Dokmeci, A. Khademhosseini, *Adv. Mater.* **2016**, *28*, 3280.
- [16] D. T. Simon, E. O. Gabrielsson, K. Tybrandt, M. Berggren, *Chem. Rev.* **2016**, *116*, 13009.
- [17] S. S. Kim, J. H. Jeon, H. I. Kim, C. D. Kee, I. K. Oh, *Adv. Funct. Mater.* **2015**, *25*, 3560.
- [18] S. G. Hashmi, T. Moehl, J. Halme, Y. Ma, T. Saukkonen, A. Yella, F. Giordano, J. D. Decoppet, S. M. Zakeeruddin, P. Lund, M. Gratzel, *J. Mater. Chem. A* **2014**, *2*, 19609.
- [19] F. Palazon, S. Dogan, S. Marras, F. Locardi, I. Nelli, P. Rastogi, M. Ferretti, M. Prato, R. Krahne, L. Manna, *J. Phys. Chem. C* **2017**, *121*, 11956.
- [20] J. H. M. Maurer, L. González-García, B. Reiser, I. Kanelidis, T. Kraus, *Nano Lett.* **2016**, *16*, 2921.
- [21] H. Zhang, P. R. Patel, Z. Xie, S. D. Swanson, X. Wang, N. A. Kotov, *ACS Nano* **2013**, *7*, 7619.
- [22] T.-Y. Kim, M. Amani, G. H. Ahn, Y. Song, A. Javey, S. Chung, T. Lee, *ACS Nano* **2016**, *10*, 2819.
- [23] C. Tan, X. Cao, X.-J. Wu, Q. He, J. Yang, X. Zhang, J. Chen, W. Zhao, S. Han, G.-H. Nam, M. Sindoro, H. Zhang, *Chem. Rev.* **2017**, *117*, 6225.
- [24] J. Lim, X. Jin, Y. K. Jo, S. Lee, S. J. Hwang, *Angew. Chem., Int. Ed.* **2017**, *56*, 7093.
- [25] S. Wan, Q. Zhang, X. Zhou, D. Li, B. Ji, L. Jiang, Q. Cheng, *ACS Nano* **2017**, *11*, 7074.
- [26] S. Eigler, A. Hirsch, *Angew. Chem., Int. Ed.* **2014**, *53*, 7720.
- [27] S. Eigler, M. Enzelberger-Heim, S. Grimm, P. Hofmann, W. Kroener, A. Geworski, C. Dotzer, M. Röckert, J. Xiao, C. Papp, O. Lytken, H.-P. Steinrück, P. Müller, A. Hirsch, *Adv. Mater.* **2013**, *25*, 3583.
- [28] Q. Cheng, M. Wu, M. Li, L. Jiang, Z. Tang, *Angew. Chem., Int. Ed.* **2013**, *52*, 3750.
- [29] E. B. Secor, P. L. Prabhumirashi, K. Puntambekar, M. L. Geier, M. C. Hersam, *J. Phys. Chem. Lett.* **2013**, *4*, 1347.
- [30] F. J. Tölle, M. Fabritius, R. Mühlaupt, *Adv. Funct. Mater.* **2012**, *22*, 1136.
- [31] S. Li, C. Cheng, H. W. Liang, X. Feng, A. Thomas, *Adv. Mater.* **2017**, *29*, 1700707.
- [32] Y. J. Yun, W. G. Hong, W.-J. Kim, Y. Jun, B. H. Kim, *Adv. Mater.* **2013**, *25*, 5701.
- [33] Z. Liu, Z.-S. Wu, S. Yang, R. Dong, X. Feng, K. Müllen, *Adv. Mater.* **2016**, *28*, 2217.
- [34] Z.-Q. Feng, T. Wang, B. Zhao, J. Li, L. Jin, *Adv. Mater.* **2015**, *27*, 6462.
- [35] Z. Liu, K. Parvez, R. Li, R. Dong, X. Feng, K. Müllen, *Adv. Mater.* **2015**, *27*, 669.
- [36] S. Shah, P. T. Yin, T. M. Uehara, S.-T. D. Chueng, L. Yang, K.-B. Lee, *Adv. Mater.* **2014**, *26*, 3673.
- [37] E. B. Secor, S. Lim, H. Zhang, C. D. Frisbie, L. F. Francis, M. C. Hersam, *Adv. Mater.* **2014**, *26*, 4533.
- [38] E. B. Secor, B. Y. Ahn, T. Z. Gao, J. A. Lewis, M. C. Hersam, *Adv. Mater.* **2015**, *27*, 6683.
- [39] A. Naumov, F. Grote, M. Overgaard, A. Roth, C. E. Halbig, K. Nørgaard, D. M. Guldi, S. Eigler, *J. Am. Chem. Soc.* **2016**, *138*, 11445.

- [40] S. Wang, P. K. Ang, Z. Wang, A. L. L. Tang, J. T. L. Thong, K. P. Loh, *Nano Lett.* **2010**, *10*, 92.
- [41] F. Torrisi, T. Hasan, W. Wu, Z. Sun, A. Lombardo, T. S. Kulmala, G.-W. Hsieh, S. Jung, F. Bonaccorso, P. J. Paul, D. Chu, A. C. Ferrari, *ACS Nano* **2012**, *6*, 2992.
- [42] L. Ma, C. Cheng, C. He, C. Nie, J. Deng, S. Sun, C. Zhao, *ACS Appl. Mater. Interfaces* **2015**, *7*, 26050.
- [43] M. F. Gholami, D. Lauster, K. Ludwig, J. Storm, B. Ziem, N. Severin, C. Bottcher, J. P. Rabe, A. Herrmann, M. Adeli, R. Haag, *Adv. Funct. Mater.* **2017**, *27*, 1606477.
- [44] C. Fasting, C. A. Schalley, M. Weber, O. Seitz, S. Hecht, B. Koksich, J. Dernedde, C. Graf, E. W. Knapp, R. Haag, *Angew. Chem., Int. Ed.* **2012**, *51*, 10472.
- [45] J. Vonnemann, S. Liese, C. Kuehne, K. Ludwig, J. Dernedde, C. Bottcher, R. R. Netz, R. Haag, *J. Am. Chem. Soc.* **2015**, *137*, 2572.
- [46] B. Ziem, H. Thien, K. Achazi, C. Yue, D. Stern, K. Silberreis, M. F. Gholami, F. Beckert, D. Groger, R. Mulhaupt, J. P. Rabe, A. Nitsche, R. Haag, *Adv. Healthcare Mater.* **2016**, *5*, 2922.
- [47] T. A. Strom, E. P. Dillon, C. E. Hamilton, A. R. Barron, *Chem. Commun.* **2010**, *46*, 4097.
- [48] H. He, C. Gao, *Chem. Mater.* **2010**, *22*, 5054.
- [49] S. Eigler, Y. Hu, Y. Ishii, A. Hirsch, *Nanoscale* **2013**, *5*, 12136.
- [50] X. Hu, Z. Xu, C. Gao, *Sci. Rep.* **2012**, *2*, 767.
- [51] S. Abdolhosseinzadeh, H. Asgharzadeh, H. Seop Kim, *Sci. Rep.* **2015**, *5*, 10160.
- [52] A. Faghani, I. S. Donskyi, M. Fardin Gholami, B. Ziem, A. Lippitz, W. E. S. Unger, C. Böttcher, J. P. Rabe, R. Haag, M. Adeli, *Angew. Chem., Int. Ed.* **2017**, *56*, 2675.
- [53] Z. Qi, P. Bharate, C.-H. Lai, B. Ziem, C. Böttcher, A. Schulz, F. Beckert, B. Hatting, R. Mülhaupt, P. H. Seeberger, R. Haag, *Nano Lett.* **2015**, *15*, 6051.
- [54] H. Onoe, T. Okitsu, A. Itou, M. Kato-Negishi, R. Gojo, D. Kiriya, K. Sato, S. Miura, S. Iwanaga, K. Kuribayashi-Shigetomi, Y. T. Matsunaga, Y. Shimoyama, S. Takeuchi, *Nat. Mater.* **2013**, *12*, 584.
- [55] Z. Li, J. T. Zhang, Y. M. Chen, J. Li, X. W. Lou, *Nat. Commun.* **2015**, *6*, 8850.
- [56] H.-C. Tian, J.-Q. Liu, D.-X. Wei, X.-Y. Kang, C. Zhang, J.-C. Du, B. Yang, X. Chen, H.-Y. Zhu, Y.-N. NuLi, C.-S. Yang, *Biomaterials* **2014**, *35*, 2120.
- [57] K. Hu, J. Sun, Z. Guo, P. Wang, Q. Chen, M. Ma, N. Gu, *Adv. Mater.* **2015**, *27*, 2507.
- [58] K. Minami, Y. Kasuya, T. Yamazaki, Q. M. Ji, W. Nakanishi, J. P. Hill, H. Sakai, K. Ariga, *Adv. Mater.* **2015**, *27*, 4020.
- [59] A. Solanki, S.-T. D. Chueng, P. T. Yin, R. Kappera, M. Chhowalla, K.-B. Lee, *Adv. Mater.* **2013**, *25*, 5477.